Computational fluid dynamics simulations of flow and dispersion in the aerosol test chamber

Hannibal E. Fossum and Bjørn A. P. Reif

Norwegian Defence Research Establishment (FFI)

19 October 2012

FFI-rapport 2012/01030

1203

P: ISBN 978-82-464-2127-8
E: ISBN 978-82-464-2128-5

Keywords

Aerosoler

Aerosolkammer

Computational Fluid Dynamics

Large Eddy Simulation

Spredning

Stokes-tallet

Approved by

Janet Martha Blatny	Project Manager
Jan Ivar Botnan	Director

English summary

This report presents findings from computer simulations of the air flow and the dispersion of aerosols inside a rectangular 12 m^3 Aerosol Test Chamber. Methodologically, the Large Eddy Simulation approach is used, in conjunction with both a scalar (Eulerian) and a discrete (Lagrangian) aerosol model. In the context of these two approaches, the Stokes number is discussed. Also, computations of dimensionless frictional l_+ distance values are reported, to check the adequacy of the mesh resolution. Furthermore, the report focuses on velocity data and dispersion results.

It seems that the Large Eddy Simulation approach is well suited for investigations of the flow and dispersion in the Aersol Test Chamber. From an operational point of view, the findings of the present study suggest that the chamber does not seem optimal for studies of long-term effects (i.e. hours or more) of external conditions on aerosols, because of the decay of aerosol concentration, which is unavoidable due to gravitational settling, air circulation, particle deposition, or a combination of these factors.

Moreover, the results suggest that the design of the feedback control loop responsible for controling the aerosol injection into the chamber must be considered thoroughly in order to strike a good balance between obtaining stable concentration values as well as sufficient mixing in the chamber. Also, experimental measurements conducted in the chamber must be carried out in a particularly careful manner, if statistically valid experimental data are desired.

Sammendrag

Denne rapporten tar for seg resultater fra datasimuleringer av luftstrømning og spredning av aerosoler i et rektangulært 12 m^3 aerosolkammer. *Large Eddy Simulation*-metodikken er brukt sammen med både en Eulerisk skalarmodell og en Lagrangisk partikkelmodell for å modellere aerosolene. I den forbindelse er Stokes-tallet diskutert. Beregninger av dimensjonsløse (friksjonsbaserte) l_+-avstandsverdier er også vist, med den hensikt å undersøke beregningsnettets oppløsning. I tillegg fokuserer rapporten på hastighetsdata og spredningsresultater.

Det ser ut til å være vellykket å benytte *Large Eddy Simulation* for å undersøke strømning og spredning i aerosolkammeret. Fra et brukerperspektiv ser kammeret ut til å ikke være optimalt for studier av langtidseffekter (dvs. timer eller mer) av eksterne påvirkninger på aerosoler. Dette skyldes fallet i aerosolkonsentrasjon over tid, som er uungåelig grunnet gravitasjonseffekter, luftsirkulasjon, deponering eller en kombinasjon av disse faktorene.

Videre synes resultatene å indikere at designet av feedback-løkken som styrer aerosolinjeksjonen i kammeret må vurderes nøye for å finne en god balanse mellom å oppnå stabil konsentrasjon og samtidig opprettholde god nok blanding av aerosolene i kammeret. Eksperimentelle målinger som utføres i kammeret må også være meget gjennomtenkt og utføres planmessig dersom man ønsker statistisk verdifulle eksperimentelle data.

Contents

Preface

Abbreviations

The mathematical abbreviations $\partial_i = \frac{\partial}{\partial x_i}$ and $\partial_t = \frac{\partial}{\partial t}$ will be used in conjunction with regular index notation and Einstein's summation convention (i.e. e.g. $s_{ii} = s_{11} + s_{22} + s_{33}$ for a tensorial field s of rank 2 in $\mathbb{R}^3$). Furthermore, the following acronyms will be used throughout the text:

ATC	Aerosol Test Chamber
CFD	Computational Fluid Dynamics
DNS	Direct Numerical Simulation
FVM	Finite Volume Method
LES	Large Eddy Simulation
RANS	Reynolds-Averaged Navier-Stokes

Nomenclature

The following *physical* quantities are used throughout this report. Note that purely mathematical notation, such as physical or mathematical constants, unknown coefficients, example functions, indices or specific turbulence model parameters, are not included in the following. Quantities with index i refers to vector quantities (or tensors if in combination with index j), whereas index n refers to some other counting procedure. Dimensions are as listed below, except when stated otherwise in the text.

Roman Symbols

c	scalar field
d	distance to closest wall (m)
d_p	particle diameter (m)
F_D	specific Stokes drag force on a particle (1/s)
F_{x_p}	virtual mass and pressure gradient forces on a particle (m/s^2)
g_{x_p}	gravitational acceleration component in the x_p direction (m/s^2)
L	(characteristic) length scale (m)
ℓ	large-scale turbulence length scale (m)
l_+	dimensionless distance (friction-velocity based) (1)
p	total pressure field (kg/ms^2)
P	filtered pressure field (kg/ms^2)
Re	the Reynolds number (1)
S_{ij}	rate of strain (m^2/s^2)
Sc_T	the turbulent Schmidt number (1)

T	(characteristic) time scale (s)
$\mathcal{T}$	Kolmogorov time scale (s)
t	time (s)
U	(characteristic) velocity scale (m/s)
u_i	total velocity field (m/s)
U_i	filtered velocity field (m/s)
u_i'	residual velocity field (m/s)
u_p	particle velocity in the x_p direction (m/s)
u_{x_p}	fluid velocity in the x_p direction (m/s)
u_*	friction velocity (m/s)
V_{cell}	volume of a given computational cell (m^3)
$\mathcal{V}$	domain of a given computational cell
$\boldsymbol{v}$	velocity vector (m/s)
v_n	velocity normal to a cell face (m/s)
x_i	spatial coordinates in $\mathbb{R}^3$ (m)
x, y, z	spatial (Cartesian) coordinates (m)
x_p	direction tangent to a particle trajectory (m)
y_+	dimensionless distance from the wall (friction-velocity based) (1)

Greek Symbols

α_c	scalar diffusivity (m^2/s)
η	Kolmogorov length scale (m)
μ	(dynamic) viscosity of air (kg/ms)
ν	kinematic viscosity of air (m^2/s)
ν_T	residual eddy viscosity (m^2/s)
ρ	density of air (kg/m^3)
ρ_p	particle density (kg/m^3)
τ_{ij}	residual stress (m^2/s^2)
τ_{w}	wall shear stress (wall friction) (kg/ms^2)

1 Introduction

When investigating certain aspects of bioaerosols, it is often useful to keep the aerosols suspended in air for long periods of time. FFI has recently installed an air chamber (Aerosol Test Chamber, produced and delivered by Dycor Technologies Ltd., Canada) in which bioaerosols are dispersed in air. In order to evaluate the applicability of the chamber to long-term investigations of bioaerosols, numerical simulations of the flow inside the chamber are desired.

Inside the chamber, the air is supposed to flow in such a way as to enhance mixing and minimize the effect of gravitational settling on the bioaerosols, thus keeping them suspended in the air for a long time. Among other things, it is of interest to understand how long bacteria carried by the wind field remain alive. One might want to expose these so-called bio-aerosols to certain external conditions (e.g. temperature, humidity or radiation) and then measure how the bacteria respond to such treatment. Also within the fields of chemistry, radiation physics, and meteorology, the continuous suspension of aerosols in air is relevant.

A number of approaches have been developed and refined over the last decades in order to achieve long-term suspension of aerosols in air, e.g. designs such as the rotating drum (Frostling, 1973) or the vertical cylinder (Marple and Rubow, 1983). In the present study, one such design will be explored, namely the Aerosol Test Chamber (ATC), a $3 \times 2 \times 2$ m^3 air chamber delivered by Dycor (Dycor Technologies Ltd.; ATC-12). According to the manufacturer, the chamber allows relatively tight control of temperature, humidity and other external conditions, while aerosols can be injected into the chamber for long-term suspension.

Little or no research has, however, been done to characterize and quantify the flow patterns inside the ATC, experimentally or computationally. Moreover, to the knowledge of the authors, there are no studies detailing how long aerosols may remain suspended within the chamber. In fact, very little information seems to exist altogether on how the chamber performs with respect to flow and dispersion. This constitutes the primary motivation for this study.

In order to assess the suitability, usefulness and quality of the Aerosol Test Chamber (ATC) at FFI, knowledge about the airflow inside the chamber is desired. Such knowledge can be gathered through a variety of experiments, by means of Computational Fluid Dynamics (CFD), or through a combination of the two. The former approach, using Particle Imaging Velocimetry or Laser Doppler Anemometry, is expensive and rather time-consuming, whereas the latter method is cheaper and often faster. However, the results from the computational approach ought to be verified by a select group of experiments to attain general validity.

The present report focuses on how the CFD methodology can be used to predict the flow fields inside the ATC. The preparations and assumptions behind the computational model, the results of the computer simulations, and the validity of the results will be discussed.

1.1 Aims

The main goal of the present study as a whole is to obtain information about the flow field and aerosol dispersion inside the ATC, by use of CFD. More specifically, this report will discuss, among other,

- the computational methodology used to simulate flow and dispersion in the chamber and its suitability,
- important characteristics of the flow which influences aerosol dispersion simulations, e.g. reports of the Stokes number,
- aspects of the flow field inside the ATC, and
- key results from dispersion simulations.

In the concluding remarks, special emphasis will be placed on the practical relevance and implications of the findings from this study for an experimentalist using the ATC.

1.2 Computational Fluid Mechanics

In the present report, a commercial CFD code is employed (ANSYS Fluent 12.1). The code solves filtered conservation equations for momentum and mass, as well as additional model equations, in a Finite Volume framework (Fluent User's Guide).

Using CFD to simulate flow in closed systems such as pipes, tanks or chambers is not a new idea. The general methodology has been used in the industry for about half a century, although with increasingly more complex models. Often, one assumes the flow to be statistically steady and therefore adopts e.g Reynolds-Averaged Navier-Stokes modeling.

In the case of aerosol dispersion, the fluctuations in the pressure and velocity fields will influence the aerosol mixing significantly, and therefore it is important to resolve the fluctuations as accurately and correctly as possible. Consequently, turbulence models which only provide the mean flow fields are not ideal. Instead, the Large Eddy Simulation (LES) model is used in the present study, a model in which the larger scales of turbulence are fully resolved, while only the smaller scales are modeled. This implies that time-dependent fluctuating velocity and pressure fields are computed.

The LES model is not recommended for flows primarily governed by wall-generated turbulence, since it then requires a very fine near-wall resolution (George and Tutkun, 2009). However, the bulk of the turbulence production in the chamber arises from free-shear flow phenomena, especially at the edges of the flow jets which are generated in front of the two circulation fans situated in the chamber. Thus, the selected LES approach seems an appropriate choice for the present case.

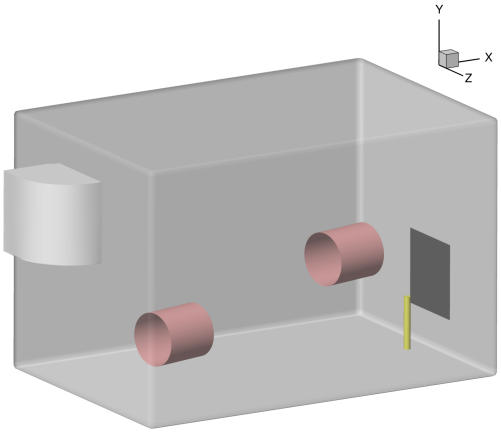

(a) The model geometry of the ATC. The cirulation fans are marked in red, the particle injector is marked in yellow. The inlet is marked by a darker area at the right wall, whereas the outlet is shown on the left wall.

(b) A picture of the ATC at the Norwegian Defence Research Establishment (FFI).

Figure 2.1 The Aerosol Test Chamber.

2 Problem Characterization

The Aerosol Test Chamber (ATC) is shown in Figure 2.1. Its dimensions are $3 \times 2 \times 2$ m^3 and it is equipped with two circulation fans. These are faced toward each other, but with their axes slightly offset. Measuring equipment can be mounted inside the chamber through a number of ports in the bottom of the chamber. In the present study, only the aerosol injection pipe and the two fans are modeled. The omission of measuring equipment in the model is however not believed to significantly impact the results or the general validity of the results.

Some key features of the chamber, as well as other relevant problem parameters, are given in Table 2.1 on the following page. The aerosol mass density and sizes are specified based on actual aerosols used in the real chamber. It has been assumed throughout this study that the aerosols remain spherical as they are dispersed inside th ATC. This is a fairly good approximation for the small aerosol sizes considered in this study.

3 Computational Modeling

3.1 Mesh Generation

A hexahedral mesh with $4.8 \cdot 10^6$ cells was generated. Figure 3.1 shows the surface mesh density of the circulation fans, as well as three of the chamber walls. When creating the mesh, care was taken that the cell sizes did not vary too rapidly in space, particularly in dynamically important regions; large mesh size gradients generally reduce numerical stability, and in this particular case

Dimensions	3.0 m $\times$ 2.0 m $\times$ 2.0 m = 12 m^3
Chamber flow-through (ventilation on)	0.0764 m^3 s^{-1}
Fan size	$l_{\text{fan}} = 0.4247$ m, $r_{\text{fan}} = 0.4024$ m $\Rightarrow V_{\text{fan}} = 0.2160$ m^3
Fan angle (relative to side walls)	12° horizontally, 0° vertically
Fan speeds (computed volume average)	$v_{\text{fan}} = 1.75$ m s^{-1}
Aerosol mass density	998.2 kg m^{-3}
Aerosol diameter	2 μm
Injection time	10 s
Injection velocity	6 m s^{-1}

Table 2.1 Physical characteristics of the ATC.

details of the flow were important everywhere.

Cell edge lengths typically lay around 15–20 mm. As already mentioned, the turbulence is not wall-driven in the present problem, so the near-wall resolution was not as critical as in e.g. pipe flow. Nevertheless, and partly to accomodate potential deposition simulations at a later stage, the near-wall resolution was kept around 1 mm, yielding dimensionless distances (based on the friction-velocity), denoted y_+, mainly in the range $1 < y_+ < 15$, with some small regions of larger values close to the inlets and outlets of the circulation fans.

The dimensionless distance y_+ describes the ratio between the physical size of the computational grid and the smallest possible turbulence scales in the flow.

From a consideration of scales, it is known that the ratio of the largest turbulence scales ℓ to the smallest scales η (the Kolmogorov scale) is $\ell/\eta \sim {\text{Re}_{\text{t}}}^{3/4}$. The turbulence Reynolds number Re_{t} can be estimated by $\text{Re}_{\text{t}} \lesssim \text{Re} = UL/\nu$, where U and L are characteristic velocity and length scales, respectively, and ν is the kinematic viscosity of air.

In the present case, an estimate of the characteristic scales is $L \sim 2r_{\text{fan}} \approx 0.8$ m, $U \sim v_{\text{exhaust}} \approx 3$ ms^{-1}, where v_{exhaust} is the typical fan jet velocity directly in fron of the fans (see Section "Boundary Conditions"), implying $\text{Re} = 1.7 \cdot 10^5$. Furthermore, one can estimate that $\ell \sim L$ which altoghether yields $\Rightarrow \eta \sim 4 \cdot 10^{-4}$ m. By similar arguments, the smallest turbulence time scale can be estimated as $\mathcal{T} \sim 10^{-3}$. This implies that the smallest turbulent eddies are approximately 0.5 mm and fluctuates with a frequency (τ^{-1}) of approximately 1000 Hz.

Now, a comparison can be made between the cell sizes in the computational mesh, Δx_{cell} and the smallest turbulence scales estimated above, η, i.e. $\Delta x_{\text{cell}}/\eta$. This ratio indicates that our present mesh contains cell sizes in the range $\sim (3\eta, 60\eta)$, i.e. it is quite finely resolved[1].

[1]Cell sizes $\lesssim \eta$ would push the LES simulation towards a DNS (subject to numerical accuracy), i.e. the effect of the sub-grid-scale model would diminish, whereas sizes $\gg \eta$ would push the LES simulation towards a RANS-like result. The latter limit is however not recommended.

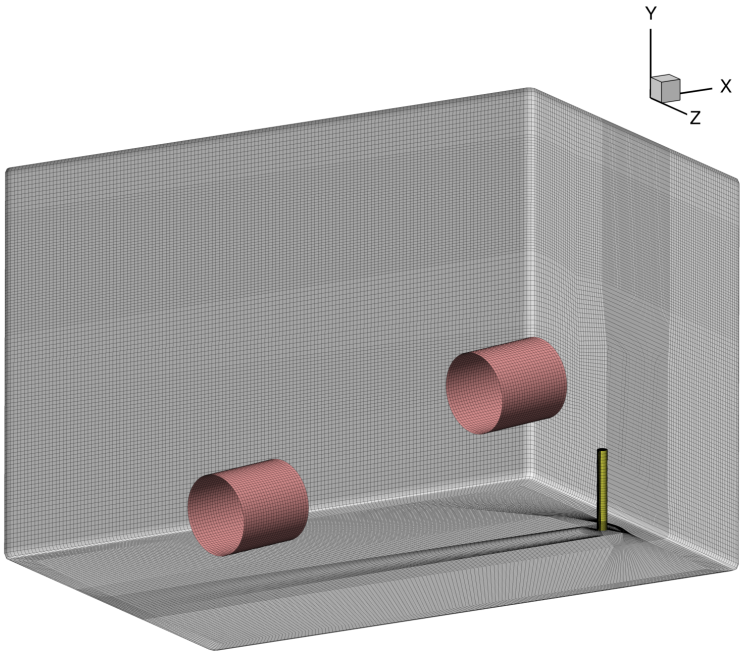

Figure 3.1 The computational surface mesh inside the Aerosol Test Chamber, including the two fans. The fans face each other, but with an offset with respect to their axes.

Moreover, the estimate of $\Delta x_{\text{cell}}/\eta$ serves as an estimate of

$$l_+ = \max(\Delta x_{i,\text{cell}})u_*/\nu \sim \sqrt[3]{V_{\text{cell}}}\sqrt{|S|/\nu} \tag{3.1}$$

in which ν is the kinematic viscosity, $|S|$ is the norm of the rate-of-strain tensor, V_{cell} is the computational cell volume, and $u_* = \sqrt{\max(\partial U_i/\partial x_j)\nu}$ is a measure of the friction velocity. l_+ is a non-dimensional length scale similar to the frictional scale y_+ used for wall-bounded flows.

The three-dimensional l_+ field is reported in the "Results" section in order to verify the $\Delta x_{\text{cell}}/\eta$ estimates above and thus verify the adequacy of the mesh resolution.

3.2 Turbulence Modeling

The LES model, utilizing the dynamic Smagorinsky approach, has been used in this study, as implemented in the commercial software ANSYS Fluent 12.1 (Fluent User's Guide). A general understanding of the fluid mechanical conservation equations, as well as the LES approach, is assumed in the present report. For a clear and thorough introduction to these concepts, see e.g. Pope (2000) or Wyngaard (2010).

The LES filtering operation is in the following denoted by and overbar. In the special cases of the velocity and pressure fields, the filtered fields are abbreviated with capital letters, i.e. $\overline{u}_i = U_i$ and $\overline{p} = P$. The residual (sub-grid) fields are denoted with dashes, i.e. e.g. u_i' for the residual

velocity.

For a Newtonian, incompressible flow, the filtered equations for conservation of momentum and mass can be written as

$$\frac{\partial U_i}{\partial t} + U_j \frac{\partial U_i}{\partial x_j} = -\frac{1}{\rho}\frac{\partial P}{\partial x_i} + \nu \frac{\partial^2 U_i}{\partial x_j \partial x_j} - \frac{\partial \tau_{ij}}{\partial x_j}, \tag{3.2}$$

$$\frac{\partial U_i}{\partial x_i} = 0, \tag{3.3}$$

respectively. $U_i(\mathbf{x}, t)$ and $P(\mathbf{x}, t)$ denote the filtered velocity component in the x_i direction and the filtered pressure field, respectively. $\tau_{ij} = \overline{u_i' u_j'} - U_i U_j$ is the *residual stress* or *sub-grid stress* tensor, which represents the impact of the unresolved velocity components (u_i) on the computationally resolved velocity field. ρ denotes the mass density of air, and ν is the kinematic viscosity of air, as defined earlier.

The present study utilizes the (dynamic) Smagorinsky model (cf. e.g. Kim, 2004), given by

$$\tau_{ij} - \tfrac{1}{3}\tau_{kk}\delta_{ij} = -2\nu_t \overline{S}_{ij}, \tag{3.4}$$

where $\nu_t = L_s^2 |\overline{S}|$ is the sub-grid (residual) turbulent viscosity. The length scale is $L_s = \min(\kappa d, C_s V^{1/3})$, where κ is the von Kármán constant, d is the distance to the closest wall, and V is the volume of the computational cell. The Smagorinsky constant C_s is determined dynamically and is computed based on the resolved scales of motion. The rate-of-strain tensor for the resolved scale is given by $\overline{S}_{ij} = \frac{1}{2}(\frac{\partial U_i}{\partial x_j} + \frac{\partial U_j}{\partial x_i})$. Note that the isotropic part of the sub-grid scales, $\frac{1}{3}\tau_{kk}\delta_{ij}$, is not modeled, as it is incorporated into the filtered pressure field.

3.3 Dispersion Modeling

3.3.1 Eulerian Framework

The transport of a passive contaminant is governed by the advection-diffusion equation

$$\frac{\partial c}{\partial t} + U_i \frac{\partial c}{\partial x_i} = \nabla^2 (\alpha_c c + \frac{\nu_T}{Sc_T} c), \tag{3.5}$$

where $c = c(\boldsymbol{x}, t)$ represents the scalar field, α_c denotes the scalar molecular diffusivity, and the last term represents a model for subgrid-scale turbulent diffusion.

In the present study, the subgrid-scale turbulent Schmidt number Sc_T is obtained through the dynamic procedure described in Germano et al. (1991).

3.3.2 Lagrangian Framework

The discrete particle transport model incorporates inertia and gravity effects inherently ignored by the scalar transport model, as well as drag forces arising from the relative motion between the aerosols and the air. The displacement of a given particle follows from integrating the force

balance on that particle, which can be written in a Lagrangian reference frame. For example, in the tangential direction x_p of the particle trajectory, the force balance can be written (after dividing both sides of the equation by the particle mass) as

$$\frac{\mathrm{d}u_p}{\mathrm{d}t} = F_D(u_{x_p} - u_p) + \frac{g_{x_p}(\rho_p - \rho)}{\rho_p} + F_{x_p}, \tag{3.6}$$

where u_{x_p} and u_p is the fluid and particle velocity, respectively, in the x_p direction. The former is obtained from the LES flow field. F_D denotes the drag force in the x_p direction on the particle exerted by the wind field, ρ and ρ_p are the densities of the fluid and the particle, respectively, and g_{x_p} is the gravitational acceleration in the x_p direction. F_{x_p} takes into account pressure-gradient and virtual-mass effects, i.e.

$$F_{x_p} = \frac{1}{2}\frac{\rho}{\rho_p}\frac{\mathrm{d}}{\mathrm{d}t}(u_{x_p} - u_p) + \left(\frac{\rho}{\rho_p}\right) u_{p,i}\frac{\partial u_{x_p}}{\partial x_{p,i}}. \tag{3.7}$$

The drag force is modeled using a spherical drag law, i.e.

$$F_D = \frac{18\mu}{\rho_p d_p^2}\frac{C_D \mathrm{Re}_{\mathrm{slip}}}{24}. \tag{3.8}$$

Here, d_p is the diameter of the particle, and C_D is the drag coefficient, in the present study given by $C_D = a_1 + a_2/\mathrm{Re} + a_3/\mathrm{Re}^2$. The constants a_1, a_2 and a_3 apply to smooth spherical particles over several ranges (Morsi and Alexander, 1972). Also in the above, $\mathrm{Re}_{\mathrm{slip}}$ is the slip velocity Reynolds number, defined as $\mathrm{Re}_{\mathrm{slip}} \equiv \rho d_p |u_p - u_{x_p}|/\mu$, where μ and ρ are the (dynamic) viscosity and mass density (as defined earlier) of air, respectively.

In its original form, integration of Eq. (3.6) only yields the particle velocity based on the resolved scales of motion. To account for the sub-grid scales, a stochastic model is applied, through which a fluctuating velocity component is added to the fluid velocity used in Eq. (3.6) at every time step. The fluctuating velocity components are discrete piecewise constant functions of time. Their random value is kept constant over an interval of time given by the characteristic lifetime of the eddies, computed from the resolved field.

In this study, thermophoretic forces, brownian forces, and lift forces are assumed to be insignificant and are therefore neglected. Also, effects such as evaporation, agglomeration, and particle collisions are neglected, as are all effects of the particles on the surrounding fluid. The particle release in this study can be considered dilute, making these simplifying assumptions approximately valid (Elgobashi, 1994).

3.3.3 Particle Inertia

Although the discrete particle model makes the most physical sense, the scalar model has an advantage in that it provides a continuous solution in the entire fluid domain. In the limit of infinitely many infinitely small particles, the discrete model approaches the scalar model. The scalar model is valid when the particle relaxation time is very small in comparison to the

characteristic time scale of the fluid, i.e. for very small Stokes numbers, $\mathrm{St} = \tau_p/t_f \ll 1$, where $\tau_p = d_p^2\rho_p/18\mu$ is an estimate of the particle relaxation time (Hinds, 1999, p. 111), and $t_f = (2S_{ij}S_{ij})^{-1/2}$ is an estimate of the (local) fluid time scale, based on the strain rate

$$S_{ij} = \frac{1}{2}\left(\frac{\partial u_i}{\partial x_j} + \frac{\partial u_j}{\partial x_i}\right)$$

computed from the resolved scales of motion.

Physically, the Stokes number is a measure of how quickly a particle reacts to changes in the surrounding flow. For $St \ll 1$, the scalar approach is formally equivalent to the discrete particle approach. In practice, small Stokes numbers suggest that the particle mass has negligible effect on the particle trajectory, i.e. the particles are convected as a passive scalar quantity.

In the present study, the characteristic length and velocity scales are estimated as $L \sim 2r_{\mathrm{fan}} \approx 0.8$ m, $U \sim v_{\mathrm{exhaust}} \approx 3$ ms^{-1}, implying a characteristic time scale of $T = L/U \sim 10^{-1}$ s. This in turn leads to a typical Stokes number of $St \sim 10^{-4} \ll 1$, motivating the use of the scalar model. This estimate will be verified.

3.4 Numerical Approach

The pressure-based solver in Fluent has been used, and further details of the following can be found in the software documentation (Fluent User's Guide). The second-order accurate Bounded Central-Differencing scheme has been used for the momentum equations. The pressure-velocity coupling was handled by the SIMPLE scheme. A second-order implicit Euler temporal scheme was used.

The Lagrangian transport equations are integrated through a combination of a lower order implicit Euler scheme, which is unconditionally stable, and a higher-order semi-implicit trapezoidal scheme. An automated switch determines which scheme to use, depending on how far a given particle is from hydrodynamic equilibrium at a given time step.

The temporal resolution, Δt, was estimated using the characteristic time scale, i.e. $T = L/U \sim 10^{-1}$ s, where the characteristic quantities are as defined earlier. The time step was set on the conservative side of T, as $\Delta t = 0.01$ s $\sim 0.1T$. Note that according to our earlier estimates of the smallest turbulence time scale, our chosen time step corresponds to $\Delta t \sim 10\mathcal{T}$. The temporal resolution thus corresponds well with the spatial resolution, in context of the smallest turbulence scales.

Each time step was computed through an iterative process with 20 iterations.

3.5 Boundary Conditions

For the inlet of air into the chamber, a plug flow corresponding to the volume flow indicated in Table 2.1 was used (i.e. 0.234 m s^{-1}). Turbulence was generated through a spectral synthesizer method (Smirnov et al., 2001), using a turbulence intensity of 10 %. The chamber outlet was

specified as a regular pressure-outlet with zero gauge pressure. All chamber walls were modeled with the no-slip condition.

The circulation fans were expected to be the dominating source of motion and turbulence in the chamber. To be able to simulate convection of particles and scalars through the fans, the fan volumes were defined as separate fluid zones, in which a modified source term in the momentum equation forced the flow to accelerate through the fans. The source term was specified in a local cylindrical coordinate system for each fan, transformed and implemented through the use of a User-Defined Function, i.e. C++ code which is imported into the Fluent solver. For each fan, a source term of 20 m s^{-2} was added to the axial component of the cylindrical momentum equation.

Unfortunately, no real data exists on the circulation fans; nothing was reported from the ATC manufacturer about fan blade count, rotations per minute, standard liters per minute flow-through or typical velocity profiles. Preliminary measurements have been performed in order to find the approximate magnitude of the air speed in front of the fans. These measurements indicate velocities in the 2–4 m s^{-1} range in front of the fans close to the radial center of the fan exhausts. The source term of 20 m s^{-2} given above will be shown to yield comparable velocities.

Other relevant simulation parameters retained their normal values; the viscosity of air was specified as $\mu = 1.7894 \cdot 10^{-5}$ kg $(ms)^{-1}$ and the density was set to $\rho = 1.225$ kg m^{-3}. Gravitational acceleration[2] was set to $g_i = (0, -9.81, 0)$ m s^{-2}, and the operating pressure and temperature were set to 101.325 kPa and 300 K, respectively. Isothermal conditions were also assumed.

3.5.1 Aerosol Injection

The injection of aerosols was modeled as a 10 s continuous release from the injection pipe in front of the inlet (see Figure 2.1).

For the Eulerian approach, a fluid velocity of 6 m s^{-1} was used at the pipe exit into the chamber. Concurrently, the scalar field representing the aerosol concentration was set to unity at the pipe exit. In this way the scalar field, i.e. the aerosol concentration, was convected from the pipe into the chamber.

The Lagrangian approach followed a similar pattern; a velocity of 6 m s^{-1} was coupled with the injection of 10 particles per time step (1,000 particles per second) at the injection pipe exit. The particles were initialized with a velocity matching the fluid velocity of 6 m s^{-1}. A 10 s release implies the total injection of 10,000 particles into the chamber.

[2]The gravitational acceleration is relevant only for the discrete particle model. See also Section 3.6.

3.6 Gravitational Settling

In the presence of a gravitational field, aerosols experience gravitational settling, i.e. they gradually sink toward the ground, only slowed down by drag forces. For small particles ($d_p \sim 1$ μm), this process usually takes hours to complete for a chamber of dimensions like the ATC. Hence, to include effects of gravitational settling, the time frame of the ATC simulation should ordinarily reflect this time frame.

However, in the present case, a forced circulation in the aerosol chamber is set up by using the fans. As shown in Figure 2.1, the air inlet into the chamber is located lower than the outlet from the chamber. Hence, due to requirements of mass conservation, a mean vertical air flow is established in the ATC between the lower inlet and the higher outlet. For low Stokes numbers, as is the case presently, the aerosols will be transported vertically by the moving air as well.

It can easily be shown that, given the chamber flow-through listed in Table 2.1, this mean vertical flow upwards will be greater than the terminal settling velocity for aerosols of size $d_p \sim 2$ μm. In combination with the mixing of air (and aerosols) provided by the circulation fans, this suggests that gravitational settling effects are absent[3]. The downside of having the air circulation turned on is of course that aerosols will slowly exit the chamber through the outlet.

3.7 Statistical Data

Turbulent flows are random and stochastic in nature. Hence, it is often more meaningful to discuss the statistical properties of turbulent flows, rather than one particular realization or instant in time. For statistically steady flows, the time average over a large enough time yields the same result as the ensemble average over many flow realizations (see e.g. Wyngaard, 2010).

Figure 3.2 shows how an estimate of how the time average approximates the ensemble mean as the averaging time increases for the present simulation. Statistics was collected for more than 12 000 time steps, or two minutes of simulation time. As seen from the plot in Figure 3.2, this is sufficient time for adequate statistics. As a verification, the time average for more than 24 000 time steps was also computed, and mean and root-mean-square quantities were compared with the original time-mean data. The differences were insignificant.

The correlation time can be estimated as less than the eddy turn-over time, estimated as $T = L/U = 0.1$ s, implying that the statistics is based on 1 200 uncorrelated samples in time.

4 Results

4.1 Flow Field

A realistic characterization of the flow field, i.e. results pertaining to velocity and pressure fluctuations in the chamber, are highly relevant to the operation of the ATC; it can give indications

[3] Gravitational settling effects will, however, be present when the air circulation through the chamber is turned off.

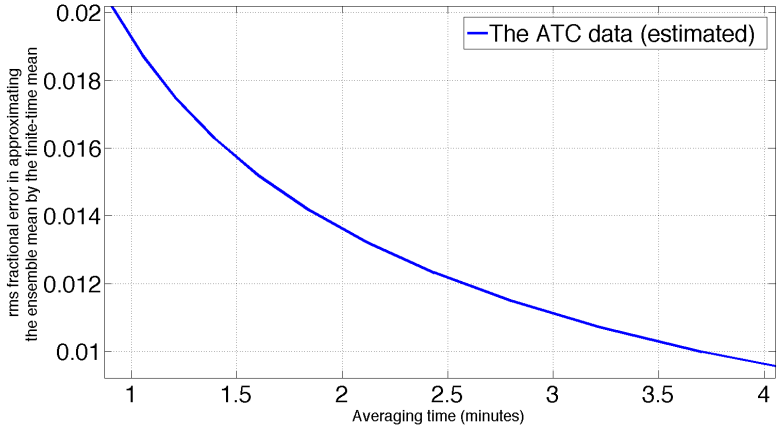

Figure 3.2 An estimate of how the temporal mean approximates the ensemble mean as averaging time increases. [rms = root-mean-square.]

of where experimental equipment (measuring devices, injection pipes, etc.) should be placed, or when and for how long various measurements should be carried out.

In this study, a qualitative assessment of the velocity field will be in focus, mainly by means of volume visualizations. Mean and root-mean-squared kinetic energy will be discussed, along with a measure of l_+. The computed wall friction will also be mentioned.

Figure 4.1 shows instantaneous l_+ values in the chamber. The bulk of the l_+ values lie in the range $(5, 30)$, remarkably close to the previous estimate (earlier sections). Such low l_+ values indicate that the mesh is indeed well-resolved relative to the flow dynamics, which adds significant credibility to the results. The highest values of l_+ are located near the edges of the fan jets, which is no surprise; this is where most of the turbulence is generated, which implies a large separation of scales.

The mean velocity magnitude is shown in Figure 4.2a. Note that the velocity in front of the fans indeed match the target velocity from the experimental measurements (cf. the "Boundary Conditions" section). It can easily be seen that the fans are the dominant source of motion in the chamber; the momentum contributions from the ventilation system (i.e. the inlet) and the particle injection pipe is close to negligible for the global flow pattern.

In the context of experimental measurements, it may be of interest to know where there are large velocity fluctuations compared to the statistical mean. This can potentially affect the required measuring time, or the required number of experiments, greatly.

Coincidentally, the ratio between root-mean-square velocities and mean velocities also shows where the turbulence kinetic energy is dominating the mean kinetic energy. Figure 4.2b shows the ratio of the root-mean-square kinetic energy $k = \frac{1}{2}U_{i,\mathrm{rms}}U_{i,\mathrm{rms}}$ to the mean kinetic energy $K = \frac{1}{2}U_{i,\mathrm{mean}}U_{i,\mathrm{mean}}$. Note how once again the edges of the jet is easy to spot in the visualization.

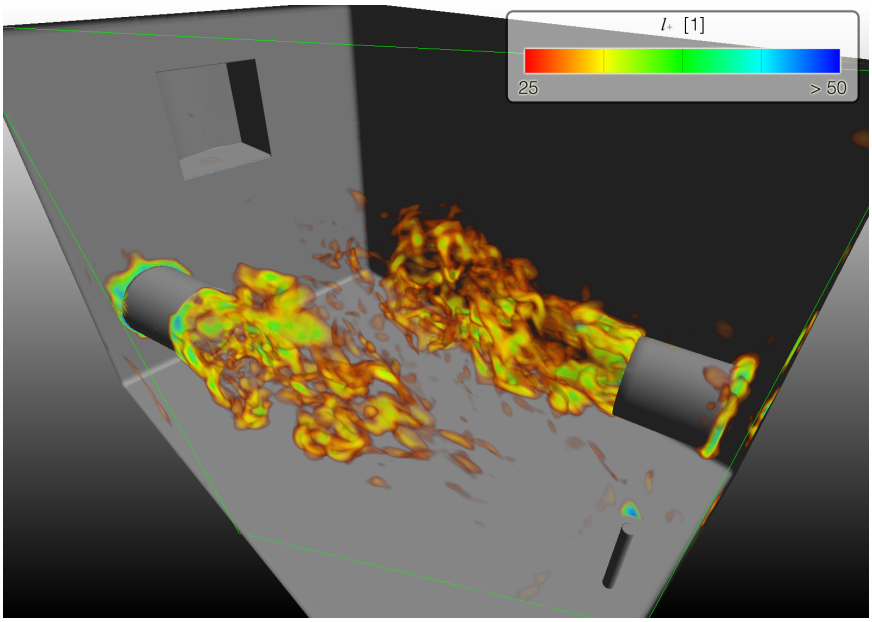

Figure 4.1 Instantaneous levels of l_+ in the ATC.

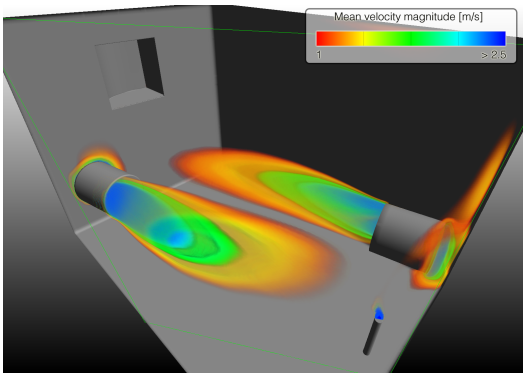

(a) Mean velocity magnitudes in the ATC.

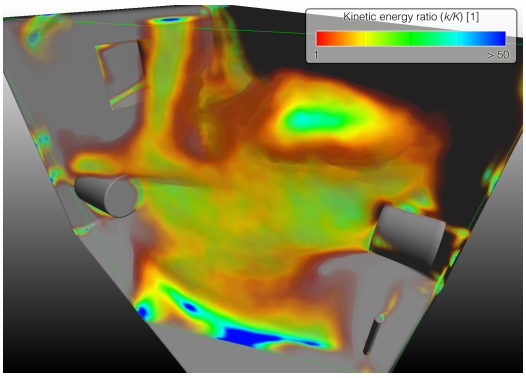

(b) The ratio of root-mean-square (rms) kinetic energy to mean kinetic energy, i.e. k/K, in which $k = \frac{1}{2}U_{i,\mathrm{rms}}U_{i,\mathrm{rms}}$ and $K = \frac{1}{2}U_{i,\mathrm{mean}}U_{i,\mathrm{mean}}$

Figure 4.2 Volume visualizations of mean velocity and kinetic energy ratio.

Even though the values of k/K inside the jet appear to be small, k itself may very well be large there – though not in comparison to K.

Independently, Figure 4.2b suggests that experimental measurements should take place in the open (transparent) region consisting of the volumes in front of the fans and between the two jets from the fans (seen in Figure 4.2a) in order to minimize the required measuring time. However, other factors may of course play a role as well, such as aerosol velocity or degree of homogeneous mixing.

In any case, it should be noted that the ratio of fluctuating to mean velocity is multiplied by a factor of 50 or more by just moving a few centimeters at certain locations in the ATC – which indicates that at certain measuring locations, these flow features should be taken seriously. Ideally, multiple simultaneous measuring locations would always be preferable.

A final flow consideration in the present report focuses on the wall shear stress, i.e. the shearing forces exerted by the air on the wall surfaces of the ATC. Certain regions of the chamber wall will be affected more by shear stress than others. Such regions of high shear are generally correlated with regions of high turbulence kinetic energy, which in turn increases the likelyhood for particle deposition – or at least particle-wall collisions. Given that higher shear also may increase re-aerosolization of particles, the net particle deposition on the wall is hard to estimate without proper models. However, if one neglects re-aerosolization, higher shear generally implies higher deposition rates.

Contours of mean wall shear stress magnitudes are shown in Figure 4.3. Friction lines are also included, i.e. field lines following the force-per-unit-length vector field given by $F_i = \partial\tau_{\mathrm{w}}/\partial x_i$, where τ_{w} is the mean wall shear stress magnitude.

Figure 4.3 illustrates the complexity of the flow in the ATC; predicting the deposition regions indicated by the shear stress contours is not trivial. Apart from some features, isolated effects of geometry and boundary conditions are difficult to spot. The singularity (zero wall friction) below the ventilation outlet is most likely caused by the jet from the right circulation fan, and there seems to be a tendency towards lower shear stresses at walls in the proximitiy of either of the jets.

A very simple estimate of the deposition pattern on the chamber walls could be to use the shear stress computations above in combination with information about the total deposition. The latter could be computed or measured through decay of total concentration in the ATC.

Pressure and vorticity structures may also provide insight into the fluid mechanics of the ATC. In the present report, however, information about these quantities is not discussed, as its significance is considered secondary to information about velocity data.

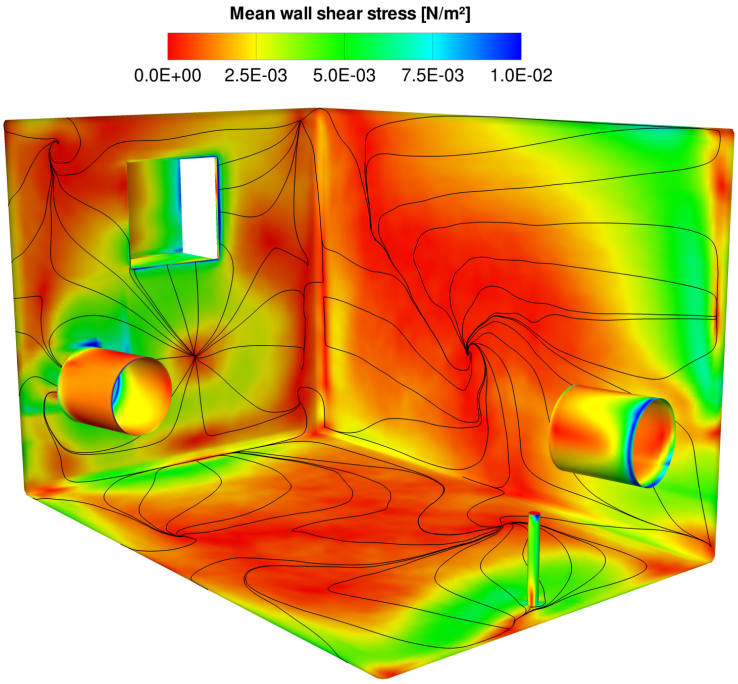

Figure 4.3 Mean wall shear stress and friction lines (field lines of $F_i = \partial\tau_w/\partial x_i$) on the walls of the ATC. Red color signifies low shear stress, blue color signifies high shear stress.

4.2 Aerosol Dispersion

4.2.1 Stokes Numbers

As discussed in a previous section, the Stokes number indicates whether or not particle inertia can be ignored. For $\mathrm{St} \ll 1$, particle inertia is negligible, whereas for $\mathrm{St} \gg 1$ particle inertia is dominant in the particle dynamics.

Although a theoretical estimate of the Stokes number was carried out a priori the simulation (see previous sections), a point-by-point computation of the Stokes number will be beneficial for future work with the ATC. Such a Stokes number field will give a more certain measure of the actual Stokes number, and the results would indicate regions where particle inertia is most likely to be a factor for heavier or larger particles in the ATC.

Figure 4.4 shows a three-dimensional visualization of the instantaneous Stokes number field in the chamber. As before, a typical water particle of 2 μm is assumed. Typical Stokes number values lie around 10^{-4}, which corresponds very well with our previous estimates. Regions of maximum Stokes number, $\mathrm{St} \gtrsim 0.002$, are colored blue, whereas regions of lower Stokes numbers, $0.001 \gtrsim \mathrm{St} \lesssim 0.002$, tends from red (lower) to yellow color. Regions of Stokes numbers less than 0.001 are not rendered, i.e. they appear invisible – this comprises most of the domain. It is clear that the Stokes number values in the ATC lie within the non-inertial particle range.

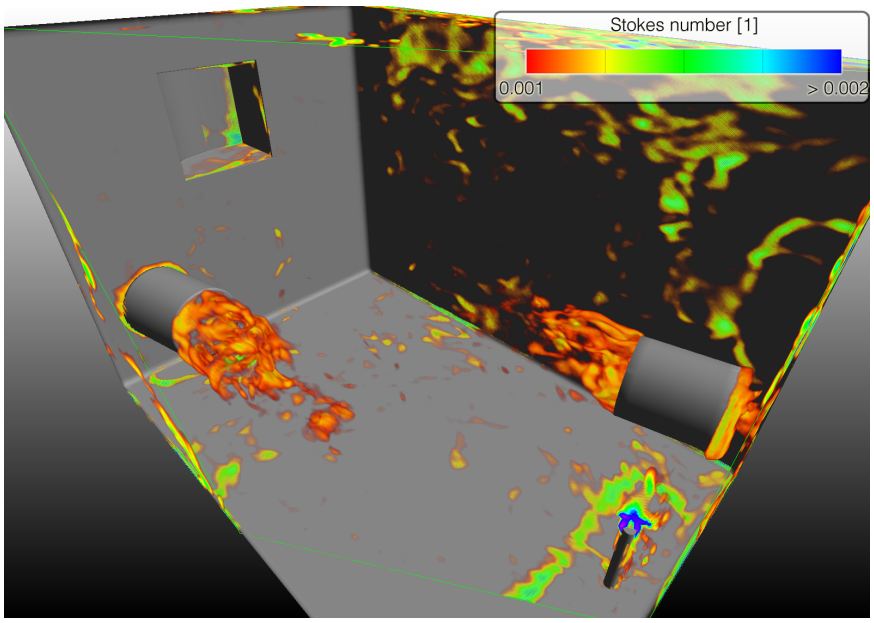

Figure 4.4 Different Stokes number regions in the ATC. Regions where $St < 0.001$ are invisible.

Not surprisingly, the Stokes number is highest in the jet in front of the circulation fans and above the particle injection pipe. This corresponds well with figure 4.2a; the velocity is high in the jets generated by the fans, resulting in a shorter fluid time scale $t_f \sim L/U$, which in turn leads to a higher Stokes number.

4.2.2 Eulerian Framework

The Eulerian approach to model aerosol dispersion, i.e. the release of a continuous gas, modeled by a scalar field, produces volumetric data which is well-suited for time-averaging, volume integration, concentration gradient calculations, contour plots and qualitative visualization.

Still images from a movie simulating the release of a scalar representing air polluted with aerosols is shown in Figure 4.7. The circulation fans seem to be mixing the scalar field quite well. As long as the ventilation system is turned on, total homogeneity will never be achieved, due to the inflow of clean air from the inlet.

The time required to reach a sufficiently homogeneous field can, however, be estimated from the simulation data, depending on a specified threshold for homogeneity. This is shown in Figure 4.5, in which the spatial root-mean-square concentration relative to the spatial mean concentration is plotted against time, where $t = 0$ s represent the beginning of the aerosol injection (not included in the figure).

Observe that the ratio remains high for at least half a minute and does not seem to stabilize until at about $t = 50$ s. At that time, the (spatial) fluctuations in aerosol concentration in the chamber appears to be roughly 3 % of the mean concentration.

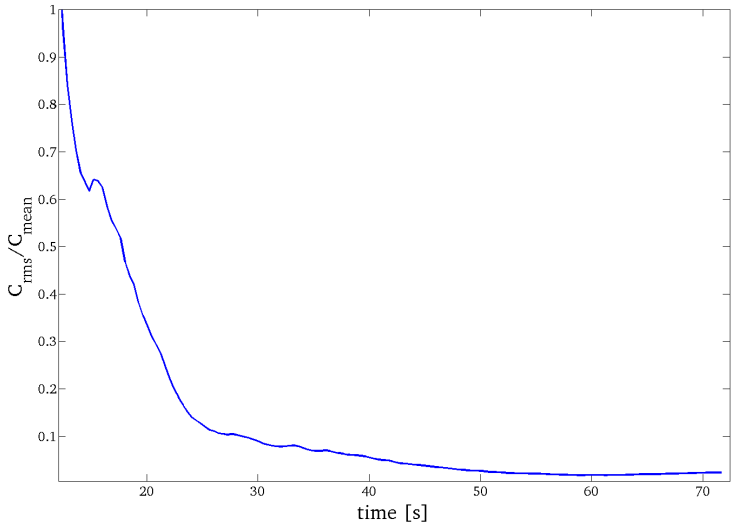

Figure 4.5 The ratio of spatially root-mean-squared concentration to spatially averaged concentration versus time for the ATC (excluding fan volumes) serves as a measure of the degree of homogeneity in the mixing of aerosols in the chamber. In the homogeneous limit, $c_{rms}/c_{mean} \rightarrow 0$.

Hence, after an aerosol injection of 10 s, one cannot assume that a single arbitrary measurement in the ATC is representative (i.e. within 3 %) of the entire aerosol field until at least 40 s after the injection has stopped. However, it is worth noting that by considering the flow/dispersion patterns in the chamber carefully, one can select certain measuring locations that might approach the true spatial mean concentration quicker than what is estimated above. Similarly, by measuring at more than one location simultaneously, one can also reduce the time required to wait for suffiently homogeneous mixing.

Figure 4.6 shows the evolution of total concentration in the chamber, normalized with the maximum concentration, which occurs at the end of the 10 s injection. Not unexpectedly, the concentration rises for the first 10 seconds, when the aerosols are injected.

After the injection, the concentration falls steadily as pure air is supplied to the chamber through the circulation chamber and polluted air exits through the outlet. However, as the concentration gets more and more dilute, the rate of decay slows down, as expected.

The plot gives an idea of how quickly the aerosols exit the ATC; within a minute after the injection terminates, the concentration is down to less than 80 %.

4.2.3 Lagrangian Framework

The Lagrangian approach to aerosol modeling has certain advantages over the Eulerian approach, as discussed earlier. However, the resulting data contains some inherent drawbacks, the most

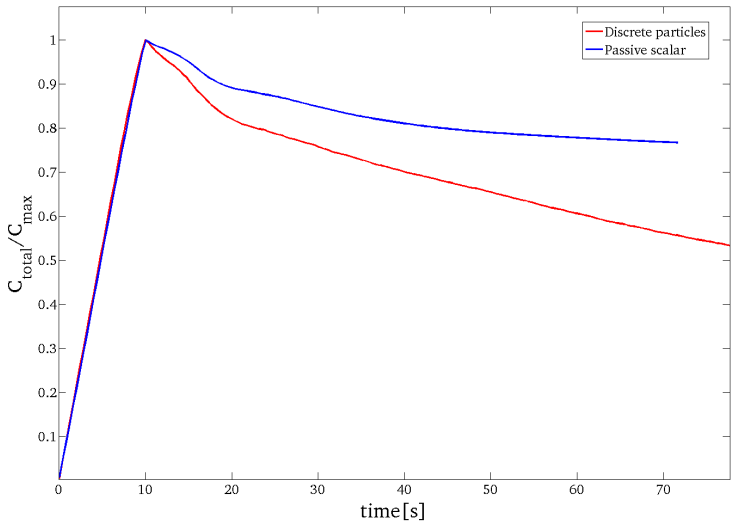

Figure 4.6 The temporal evolution of total concentration (particle count) for the passive scalar (discrete particle) dispersion model in the ATC. The injection starts at 0 s and terminates at 10 s.

significant being the lack of continuity.

One advantage of the data from a discrete particle simulation, however, is the ability to uniquely determine each particle. This enables coloring of individual particles by e.g. velocity magnitude, residence time or diameter. In Figure 4.7, the particles are colored by release time; the darkest particles are released during the first seconds of the injection, whereas the lighter particles are released later during the injection. Such a coloring gives additional information about the aerosol mixing, as one can look at how well particles released at different times have mixed after a given interval of time. This is illustrated in Figure 4.7; after 60 s, there are no discernible regions of specifically colored particles. Such analyses can be more quantified e.g. by counting particles in defined regions of the ATC, categorizing them by release time, and plotting the count versus time for each category and region.

The snapshots in Figure 4.7 show that the general trend is the same for the scalar and discrete field: During the release, the aerosols are clearly not homogeneously mixed, then gradually a more homogenous field evolves. After about a minute, the concentration has already decayed noticeably. From these preliminary looks at the data, though, it do seem like the fans have a larger effect during the injection for the scalar field simulation. This has yet to be verified quantitatively, but it is worth noting.

Figure 4.6 show the evolution of total particle count in the chamber. Not unexpectedly, the particle count rises for the first 10 seconds and then decreases, as for the Eulerian model. The count never reaches 10,000 particles, implying that aerosols starts leaving the chamber already

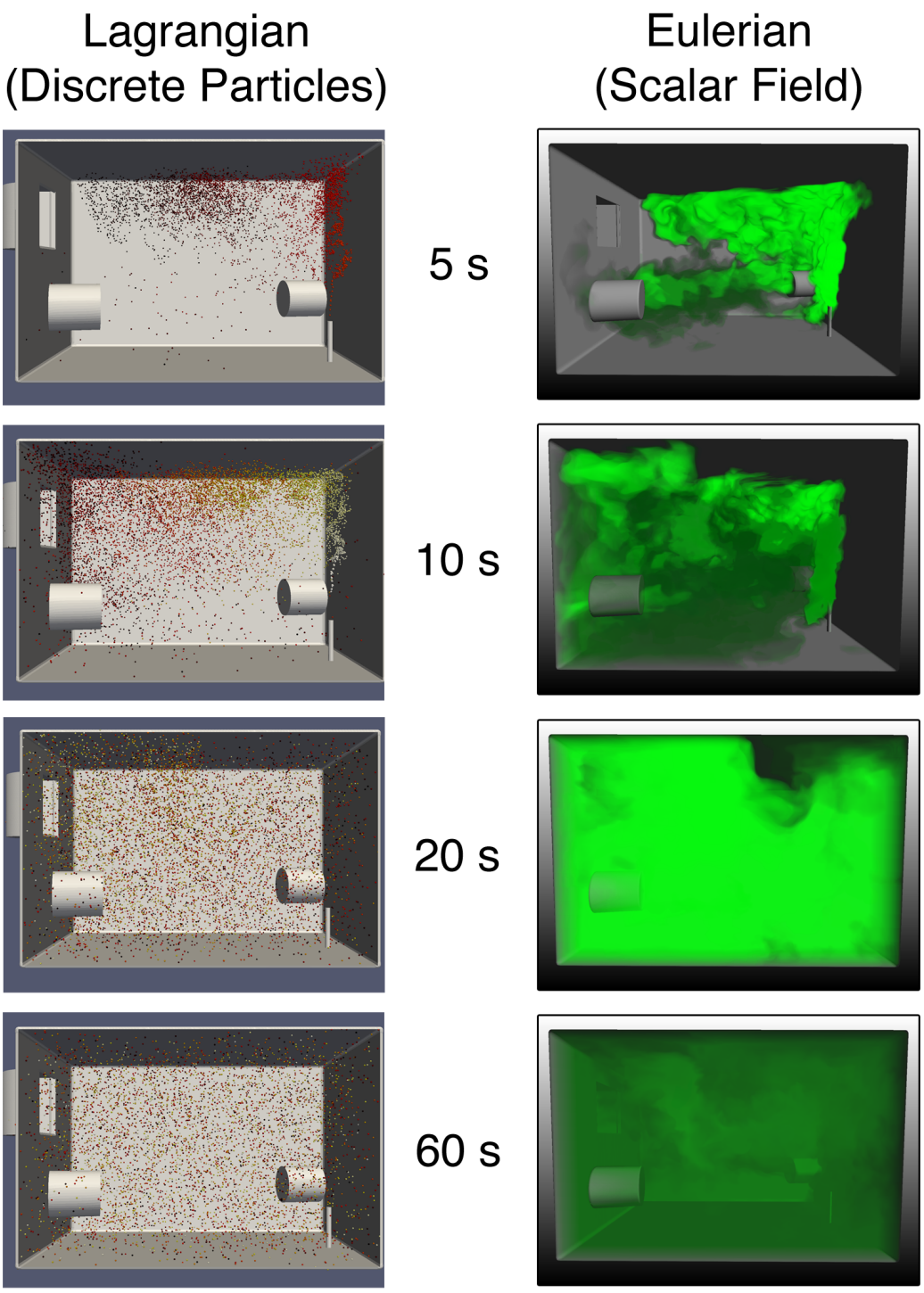

Figure 4.7 *Snapshots from the ATC simulation of aerosol injection and dispersion for a discrete particle simulation (left) and a scalar field simluation (right), in statistically similar flows. The injection starts at 0 s and terminates at 10 s.*

before the injection is terminated.

The rapid rate of decay of the Lagrangian model compared to the Eulerian model suggests strongly that 10,000 particles are not enough to represent the aerosol field appropriately in a statistical sense. This is important information for potential future studies, in which e.g. particle deposition is to be investigated.

5 Concluding Remarks

Simulations of flow and dispersion inside the ATC have been performed. These results reveal important features of the solution, in particular that

- based on the l_+ values, the computational mesh representing the ATC geometry seems adequately resolved for a detailed LES simulation, and the LES turbulence model appears to be an appropriate model,
- based on the Stokes numbers, the assumption that the aerosols can be represented by a continuous scalar field seems to hold for particles $\lesssim 2$ μm in diameter,
- there is a variability in mean shear stresses on the ATC walls, which is likely to influence particle deposition and re-aerosolization,
- the general trends in the Lagrangian and Eulerian aerosol models seem to correspond; it takes almost a minute to reach a stable degree of homogeneity in the aerosol mix (by which time the total concentration in the chamber is also significantly reduced),
- based on the Eulerian model, the concentration in the chamber decays rather quickly (it decreases to 80 % within a minute after the injection terminates) when the ventilation is turned on.

Additionally, and perhaps of the greatest importance, for the experimentalist using the chamber, the relevant findings in the present study converges to the following notable realizations:

Based on the simulations, measurements should be carried out at locations where fluctuating velocities are small compared to the mean velocities, as illustrated in Figure 4.2b. Ideally, multiple measurements should be done simultaneously at different locations.

The measurements should be taken in the shortest time possible (while still reaching a predetermined statistical convergence criteria), and they should ideally be conducted approximately 40 s after an aerosol injection, when the aerosols are (sufficiently) homogeneously mixed. The measurements should end before the next aerosol injection. Alternatively, continuous measurements can be taken over long time intervals, with subsequent removal of the sub-intervals affected by aerosol injections.

In the ATC's present configuration, there are three notable tradeoffs one needs to consider. Firstly, there is the choice of keeping the air circulation system on, which will diminish (or, at high flow rates, completely cancel out) the effects of gravitational settling. The drawback of air circulation

is, however, that aerosols will exit through the air outlet, thus preventing long-term investigations of the aerosols perhaps just as effectively as gravitational settling.

This naturally brings us to the second tradeoff in the ATC, which concerns the degree of mixing of the aerosols. Whenever new aerosols are injected into the chamber, there will be a time of inhomogeneous mixing, which in turn prevents reliable measurements. However, if injections are too dilute, too rare or too short, the total aerosol concentration will decrease steadily, due to either gravitational settling, aerosol departure through the air outlet, surface deposition, or a combination of these factors. Hence, a balance must be found, depending largely on what phenomenon and what type of aerosol one wishes to study. This means that the feedback loop controlling the aerosol injector is by no means unimportant – in fact, it might make or break the experimental measurements.

Thirdly, the circulation fans might carry an inherent tradeoff: As they increase in power (and thus blows more air), turbulence and thus mixing will increase, but so will most likely aerosol deposition inside the fans. This has not been a focus of the present study, but should nevertheless be taken into account when doing actual experiments in the ATC.

Mainly qualitative inquires have so far been made into the vast amounts of available data from the simulations. Based on the results, it seems that the LES simulation methodology is very well suited for work of this kind. Quantitative analyses, such as those birefly reported earlier in the present report, can definitely be extended to gain further insight. A comparison with experiments is also highly desirable.

5.1 Final remarks and recommendations

The ATC considered in the present study seems not to be optimal for investigations of aerosols subjected to long-term (i.e. several hours or more) external conditions, due to the tradeoff between gravitational settling and aerosol departure through the air outlet, in combination with surface deposition. For such studies, designs like the rotating drum is more appropriate.

For shorter time frames the ATC may work, if careful measurements are taken and the feedback loop is adjusted properly. However, more detailed experiments or simulations investigating the deposition rates and degree of mixing in the chamber should be carried out to be able to account properly for these effects. Also, the present study assumes a perfect aerosol injector (no deposition, completely time-independent and equally-sized aerosols in uniform concentration), which in reality will not be the case.

Acknowledgments

The visualization software VoluViz (Gaarder and Helgeland, 2002), developed at the Norwegian Defence Research Establishment (FFI), has been used for all volume visualizations in the present report. When using the VoluViz software, the assistance of Anders Helgeland is very much appreciated. Thanks are also extended to Emma Wingstedt for valuable discussions. Finally, the authors wish to thank Janet M. Blatny, who have provided general information about the various applications of the ATC.

References

Elgobashi, S. On predicting particle-laden turbulent flows. *Appl. Sci. Res.*, 52:309–329, 1994.

Fluent User's Guide. *Fluent 6.3 User's Guide*. Fluent, Inc., New Hampshire, USA, 2006.

Frostling, H. A rotating drum for the study of toxic substances in aerosol form. *Journal of Aerosol Science*, 4(5):411–419, 1973.

Gaarder, T. and Helgeland, A. VoluViz 1.0 Report. Tech. Rep. FFI/RAPPORT-2002/03449, FFI (Norwegian Defence Research Establishment), 2002.

George, W. K. and Tutkun, M. Mind the gap: a guideline for large eddy simulation. *Philosophical Transactions of the Royal Society A*, 367:2839–2847, 2009.

Germano, M., Piomelli, U., Moin, P., and Cabot, W. A dynamic subgrid-scale eddy viscosity model. *Physics of Fluids A: Fluid Dynamics*, 3:1760, 1991.

Hinds, W. C. *Aerosol Technology: Properties, Behavior, and Measurement of Airborne Particles* (John Wiley & Sons Ltd, NY, U.S.A., 1999), 2nd ed.

Kim, S.-E. Large eddy simulation using unstructured meshes and dynamic subgrid-scale turbulence models. Technical Report AIAA-2004-2548, American Institute of Aeronautics and Astronautics, 34th Fluid Dynamics Conference and Exhibit, 2004.

Marple, V. A. and Rubow, K. L. An Aerosol Chamber for Instrument Evaluation and Calibration. *American Industrial Hygiene Association Journal*, 44(5):361–367, 1983.

Morsi, S. A. and Alexander, A. J. An investigation of particle trajectories in two-phase flow systems. *J. of Fluid Mech.*, 55(2):193–208, 1972.

Pope, S. B. *Turbulent Flows* (Cambridge University Press, Cambridge, United Kingdom, 2000).

Smirnov, R., Shi, S., and Celik, I. Random flow generation technique for Large Eddy Simulations and particle-dynamics modeling. *Journal of Fluids Engineering*, 123:359–371, 2001.

Wyngaard, J. *Turbulence in the Atmosphere* (Cambridge Univ Pr, 2010).